IEEE Access
Multidisciplinary ⋮ Rapid Review ⋮ Open Access Journal

Received January 4, 2021, accepted January 19, 2021, date of publication January 25, 2021, date of current version February 9, 2021.

Digital Object Identifier 10.1109/ACCESS.2021.3054461

3-D Single- and Dual-Polarized Frequency-Selective Rasorbers With Wide Absorption Bands Based on Stepped Impedance Resonator

YIHAO WANG[1], MIN WANG[1], (Member, IEEE), ZHONGXIANG SHEN[2], (Fellow, IEEE), AND WEN WU[1], (Senior Member, IEEE)

[1]School of Electronic and Optical Engineering, Nanjing University of Science and Technology, Nanjing 210094, China
[2]School of Electrical and Electronic Engineering, Nanyang Technological University, Singapore 639798

Corresponding author: Min Wang (wangmin@njust.edu.cn)

This work was supported in part by the National Natural Science Foundation of China under Grant 61771242.

ABSTRACT A 3-D frequency-selective rasorbers (FSR) with wide absorption bands at both sides of the transmission window based on stepped impedance resonator (SIR) is presented and investigated in this article. The proposed FSR features thin thickness, wide absorption bands and lumped-element-free characteristics. The transmission channel is constructed from a parallel waveguide based on SIR to provide the transmission path and reduce the thickness of the whole structure. The absorption channel is filled with magnetic absorber to provide a wide absorption band, while meander-line in shunt connection with the absorber is used to avoid lumped components and to obtain a low insertion loss at the passband. The detailed design concept and analysis are illustrated and the fundamental operating principle of the FSR is demonstrated with the help of an equivalent circuit model (ECM). A design example is provided and it exhibits a passband at 7.1 GHz with a transmission bandwidth of 22.6% for less than 3 dB insertion loss and fractional bandwidth of 128.0% with reflectivity less than −10 dB. Moreover, one dual-polarized FSR is also designed and analyzed to generalize the design strategy. Both single- and dual-polarized prototypes are designed, fabricated, and measured to verify the design concept. Good agreement can be observed between the simulated and measured results.

INDEX TERMS 3-D frequency selective rasorber, absorber, frequency-selective surface, stepped-impedance resonator.

I. INTRODUCTION

Frequency-selective rasorber (FSR) [1], also termed as absorptive frequency-selective transmission structure (AFST) in [2]–[4] and absorptive frequency-selective surface (AFSS) in [5], [6], has attracted increasing interest due to its importance in numerous applications aiming to reduce radar cross-section (RCS) of antenna systems and to improve the communication security. The FSR structure was introduced as an idea for the first time in [11]. Unlike traditional FSS, the FSR exhibits in-band transmission and out-of-band absorption characteristics instead of reflecting the out-of-band electromagnetic (EM) waves, which can be seen as a combination of FSS and absorber. The key benefit of FSR is its ability to provide a specific transmission window and a low RCS over a wide frequency band at the same time.

In terms of their structures, the FSRs can be divided into two types. One is to use cascading multilayer 2-D frequency-selective surface (FSS) layers [10]–[24], and the other is employing 3-D structures where each unit is a multi-mode cavity [25]–[32]. In terms of performance, the FSR structures can also be divided into two types: 1) those with a one-sided absorption band with either lower or upper transmission band [5]–[7] and 2) those with a transmission band with two-sided absorption bands [2], [23]. As required in many practical FSR applications, the most important challenge is to expand the absorption bands, reduce the thickness of the whole structure and implement the polarization insensitivity

The associate editor coordinating the review of this manuscript and approving it for publication was Shah Nawaz Burokur.

at the same time. For the 2-D FSRs, most designs are constructed by stacking 2-D FSSs. The transmission bands are related to the pass band of these bandpass FSSs. The absorption bands are provided by the resistive FSS layers, which are mostly constituted by lossy components. Several designs have been proposed to achieve dual polarization characteristics [18]–[22]. However, it is difficult for 2-D FSR to expand the absorption bandwidths by using multiple resonators and their narrow absorption bands cannot meet the bandwidth requirements of many radar systems. Under these circumstances, the 3-D FSRs were proposed to overcome these drawbacks of 2D FSRs recently.

Instead of cascading a bandpass FSS with a lossy layer, the transmission and absorption paths of 3-D FSR are separated and can be designed independently. Due to this feature, they can be readily designed to widen the absorption bandwidth and reduce the insertion loss in the transmission band. The transmission window is achieved when the transmission path resonates and the length of the passband equals to $\lambda_c/2$, where λ_c is the guided wavelength at the center frequency of the passband. For the absorption path, part of the incident EM wave enters the absorption path and may be absorbed, resulting in a large insertion loss. However, this high insertion loss in the transmission window can be resolved by bypassing the lossy components at the frequency of transmission window [27]–[29]. In [2], a short-circuit in shunt connection with the source of losses was used to bypass the losses. The technique of inserting a series *L-C* circuit in front of the absorption path was introduced in [31]. At the resonant frequency of the *LC* resonator, the absorption path is short-circuited and the incident EM wave is then blocked from entering the absorption path. Low insertion loss can then be obtained within the passband of the FSR. An FSR without lumped elements was also provided in [4]. In addition, several methods to broaden the absorption bandwidth were proposed recently. Prototypes using multiple resonances were reported in [28] and [29] to realize frequency responses with wide absorption bands. Constructions based on ferrite materials were also implemented to increase the absorption bands of 3-D FSR [31], [32]. Moreover, the electrical sizes of the unit cell of 3-D FSRs are relatively small, leading to stable filtering responses over a large range of incident angles of EM waves.

It is noted that most of these 3-D FSRs mentioned above only operate under a single polarization, which further limits their applications. In [27], a 3-D FSR was designed for dual-polarization based on parallel-plate waveguides and lumped resistors. However, its absorption band is very narrow and the lumped resistors are difficult to be implemented and can introduce large soldering and assembling tolerances. To meet the requirements of practical antenna systems, a dual-polarized FSR with wide absorption bands, low insertion loss, thin profile and stable angular response is imperative to be realized.

In this article, a design of 3-D FSR based on magnetic absorber and SIR with wide absorption bands, thin thickness and lumped-component-free characteristics is initially presented for single-polarized applications. The magnetic absorber is utilized to produce a wide absorption band. The parallel-plate waveguide with SIR structure is constructed aiming to minimize the thickness of the FSR and to provide a selective transmission window inside the absorption band. Meander-line is used to subduct the lumped-elements and replace the series *L-C* circuit, resulting in a short circuit at the resonant frequency of the passband and a low insertion loss can then be achieved within the transmission band. Furthermore, based on this construction, a dual-polarized FSR employing a symmetrical structure is further proposed. Resonators for both transverse electric (TE) and transverse magnetic (TM) polarizations are accomplished by adopting two sets of parallel-strip lines that are orthogonal to each other in each unit cell. Operating principles of both prototypes are analyzed in detail with the help of equivalent circuit models (ECMs). Both single- and dual-polarized examples are demonstrated to verity the feasibility of the design methodology. The proposed FSRs feature thin thickness, wide absorption bands characteristics and no extra lumped components are required. The single-polarized practical realization exhibits a passband at 7.1 GHz with a transmission bandwidth of 22.6% and a 128.0% bandwidth with reflectivity less than -10 dB under the normal incidence. The dual-polarized design operates at the center frequency of 7.25 GHz with a passband bandwidth of 25.5% and an absorption bandwidth of about 121.1%.

The remaining of this article is organized as follows. The principle of operation is proposed and analyzed in detail along with the demonstration of an ECM in Section II. In Section III, a single-polarized, low-profile, and broadband 3-D FSR with high-selectivity is presented. Furthermore, its extension to dual-polarized design is further introduced for realizing a polarization-insensitive FSR in Section IV. Fabrication and measurements are conducted, and measured results are discussed in Section V. Good agreement is observed between the measured and simulated results. Finally, conclusion and discussion are given in Section VI.

II. STRUCTURE AND CONCEPT OF 3-D FSR BASED ON SIR

Based on the aforementioned designs [25]-[32], a 3-D FSR generally consists of independent transmission and absorption channels, as shown in Fig. 1. The incident EM wave will propagate through the transmission channel at the passband frequency and be absorbed by the lossy materials in absorption channel outside the transmission band. Therefore, we can divide the design procedure into two regions: the operating frequency band of transmission (f_t) and absorption bands (f_{a1} and f_{a2}).

A. CONFIGURATION OF THE UNIT CELL

The geometry of the proposed FSR is illustrated in Fig. 2(a). The 3-D and side view of the unit cell is also shown in the figure. The size of the unit cell is important for the overall performance of the 3-D FSR under oblique incidence. The

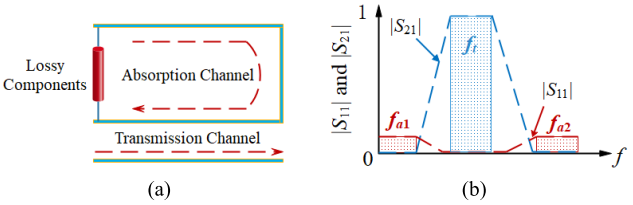

FIGURE 1. Illustration of 3-D FSR (a) Typical structure. (b) Reflection and transmission coefficients of an ideal FSR.

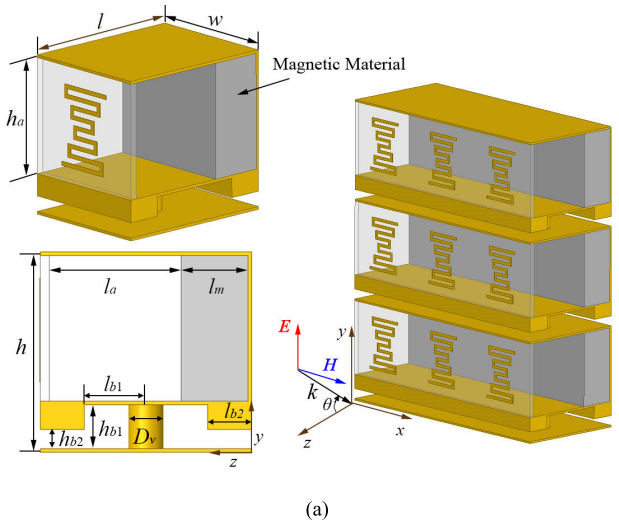

FIGURE 2. (a) 3-D view of the proposed FSR and detailed unit cell of the prototype. (b) Simulated S-parameter results of the FSR using full-wave EM simulator CST-MWS (Physical dimensions: D_v = 2 mm, h = 12 mm, h_a = 9.5 mm, h_{b1} = 2.5 mm, h_{b2} = 1.1 mm, l = 13 mm, l_a = 9 mm, l_m = 3.8 mm, l_{b1} = 4.9 mm, l_{b2} = 1.6 mm, w = 9.5 mm).

transmission channel is formed from an air path based on SIR with a metallic via in the middle. When the equivalent transmission length of the air path equals to $\lambda_t/2$, where λ_t is the guided wavelength, the transmission channel resonates at f_t and a passband can then be realized. The middle metallic via produces an additional transmission pole forming a second-order resonator, leading to a wider transmission band and a sharper roll-off for the transmission window. The diameter D_v of the via controls the coupling between these two resonant frequencies. The absorption channel is mainly constructed by a short-circuited parallel-plate waveguide filled with magnetic absorber at the end and a bypassing

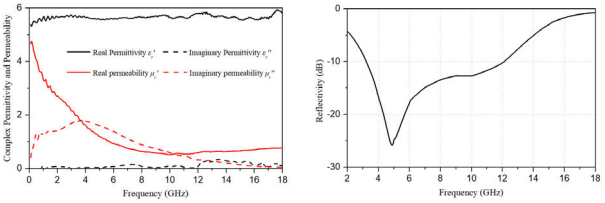

FIGURE 3. Magnetic material used in our design. (a) Complex permittivity (ε_r*) and permeability (μ_r*) and (b) Simulated reflection coefficient with back grounded.

network in the front. The air section is introduced to improve the impedance matching for better and wideband absorption. A meander line inductor in series with a gap capacitor in front of the absorption channel is designed as a band-stop FSS and employed as the bypassing network, instead of the series *L-C* circuit used in previous FSR designs. The reflection band of the absorption path is so designed to overlap with the transmission window to short-circuit the absorption path at the passband frequency. As a result, low insertion loss can then be obtained within the transmission band.

B. ABSORPTION CHANNEL FILLED WITH MAGNETIC ABSORBER

The broadband absorption effect is accomplished by the absorption channel filled with magnetic absorber partially. The complex relative permittivity ε_r^* ($\varepsilon_r^* = \varepsilon_r{}' - j\varepsilon_r{}''$) and complex permeability μ_r^* ($\mu_r^* = \mu_r{}' - j\mu_r{}''$) of the absorber used in our article are shown in Fig.3(a). The reflectivity of the conductor-backed magnetic material is shown in Fig.3(b). As a wide band absorber, the bandwidth of reflection coefficient ($|S_{11}|$) less than -10 dB is from 3.22 GHz to 12.11 GHz. Compared with those using conventional resistors, the cost of magnetic absorber is high though it has the advantage of broadband absorption. Furthermore, the magnetic absorber has high power handling capacity, which is desirable for high-power applications.

For the sake of reducing the insertion loss caused by EM waves propagating through the lossy material, the 2D band-stop FSS located at the front of the absorption path is regarded as a replacement of the series *L-C* circuit and can avoid the use of lumped components, compared with the technique described in [30]. The reflection band of the FSS is designed overlapping the transmission band, resulting in a shielded absorption path at the operating transmission frequency f_t and the incident EM waves can be blocked from propagating into the absorption path. The ECM of the absorption channel is illustrated in Fig 4.

The absorption channel can be mainly divided into three cascaded sections: one band-stop FSS and two equivalent transmission line (TL) sections ((Z_a, Θ_a) and (Z_m, Θ_m),), as shown in Fig. 4. The parallel resonator (L_f and C_f) denotes the band-stop FSS structure, while C_g represents the series capacitance between the FSS and the metal plate. The broadband magnetic absorber is demonstrated by a lossy TL. The characteristic impedances (Z_a and Z_m,) and electrical lengths

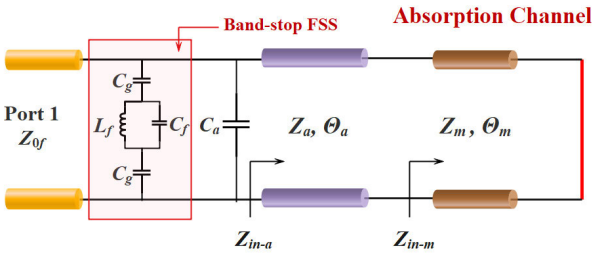

FIGURE 4. ECM of the absorption channel shown in Fig. 2.

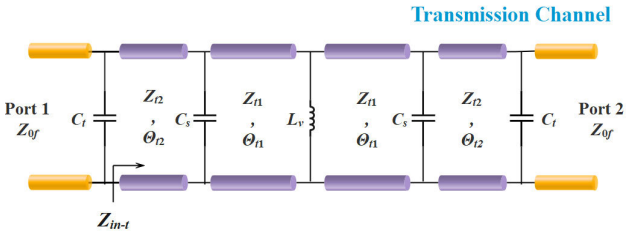

FIGURE 5. ECM of the transmission channel shown in Fig. 2.

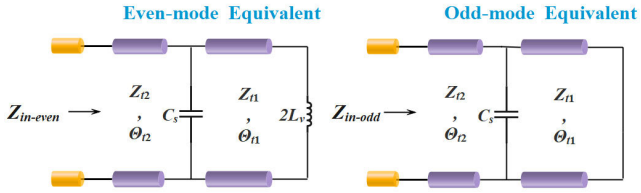

FIGURE 6. Equivalent circuits of dual-mode resonators.

(Θ_a and Θ_m,) of the air and lossy TLs are related to their physical dimensions. According to the TL theory, the relevant parameters of the absorption channel can be calculated as

$$Z_a = \eta_0 h_a / w \tag{1}$$
$$Z_m = \eta_0 h_a / w \sqrt{\mu_r^* / \varepsilon_r^*} \tag{2}$$
$$\beta_a = \omega \sqrt{\mu_0 \varepsilon_0} \tag{3}$$
$$\beta_m = \omega \sqrt{\mu_0 \varepsilon_0} \sqrt{\mu_r^* \varepsilon_r^*} \tag{4}$$
$$\Theta_i = \beta_i \times l_i, \quad i = a, m \tag{5}$$

where $\eta_0 = 120\pi\ \Omega = 377\ \Omega$ is the characteristic impedance in free space. $\omega = 2\pi f$ is the operating angular frequency. β_i ($i = a, m$) is the phase constant of each corresponding TL section.

Furthermore, the propagation constant of the lossy TL can be represented by

$$\gamma_m = j\beta_m = j\omega \sqrt{\mu_0 \varepsilon_0} \sqrt{\mu_r^* \varepsilon_r^*} \tag{6}$$

The input impedance of the lossy TL and the absorption channel can then be obtained as

$$Z_{in-m} = Z_m \tanh(\gamma_m l_m) \tag{7}$$
$$Z_{in-a} = Z_a \frac{Z_{in-m} + jZ_a \tan\Theta_a}{Z_a + jZ_{in-m} \tan\Theta_a} \tag{8}$$

Hence, the reflection coefficient ($|S_{11}|$) of the absorption channel can be expressed as

$$\Gamma_{ab} = \frac{Z_{0f} - Z_{in-a}}{Z_{0f} + Z_{in-a}} \tag{9}$$

It can be obtained that the frequencies of absorption are dependent upon the lengths of TL sections. Meanwhile, based on the equations provided above, we can also calculate different values of physical dimensions of the required FSR for pre-design and optimization.

C. TRANSMISSION CHANNEL BASED ON SIR

In the early design of the transmission channel, the parallel-plate waveguides based on uniform impedance resonator (UIR) with half guided wavelength were used mostly for the advantages of simple design and stable structure. However, in some application scenarios where compact dimensions are strictly required and the effects of the parasitic resonant frequency occurring at the integer multiples of the fundamental frequency need to be avoided, the defects and limited design parameters of the UIR structure cannot meet the demands. To reduce the physical dimension, high dielectric constant materials and lumped elements can be used in the design. For the specified substrate, the volume can be reduced by changing the geometry of the resonator. In this article, SIR structure is introduced into the transmission channel to achieve the desired thickness reduction, as shown in Fig. 2(a). It contains a wide path in the middle and one narrow path at each end. Besides, a metallic via is embedded to separate two sides of the whole path, which is responsible for producing a second-order passband. Based on this construction, the ECM of the transmission channel is then established in Fig 5.

Two sets of TL sections are included and used to describe the low- and high impedance TLs, respectively. Inductor L_v denotes the inductance of the metalized via hole, which controls the coupling coefficient. Capacitor C_s represents the step discontinuity capacitance at the interface between the narrow and wide regions in the transmission channel. C_t is the edge capacitance of the open end. $Z_{0f} = \eta_0 \times h/w$ is the port impedance. The characteristic impedances (Z_{t1} and Z_{t2},) and electrical lengths (Θ_{t1} and Θ_{t2},) can be written as

$$Z_{tj} = \eta_0 h_{bj} / w, \quad \Theta_{tj} = \omega \sqrt{\mu_0 \varepsilon_0} \times l_{tj},\ j = 1, 2 \tag{10}$$

On the basis of the corresponding equivalent TL model in Fig. 5, the symmetrical structure can be regarded as a centrally loaded resonator and divided into two symmetrical sections, each contains two TLs ((Z_{t2}, Θ_{t2}) and (Z_{t1}, Θ_{t1}),). Therefore, the two-port network can be deep analyzed by odd-even mode analytical method and elaborated into two single-port networks, as shown in Fig. 6.

The input impedances of even- and odd-mode can be expressed as

$$Z_{in-even} = jZ_{t2} \frac{R_Z \tan\Theta_{t2} + X(1 - \omega C_s Z_{t2} \tan\Theta_{t2})}{R_z - X(\omega C_s Z_{t2} + \tan\Theta_{t2})} \tag{11}$$
$$Z_{in-odd} = jZ_{t2} \frac{\tan\Theta_{t1} + R_Z \tan\Theta_{t2} - \omega C_s Z_{t2} \tan\Theta_{t1} \tan\Theta_{t2}}{R_Z - \tan\Theta_{t1} \tan\Theta_{t2} - \omega C_s Z_{t2} \tan\Theta_{t1}} \tag{12}$$

where R_Z represents the impedance ratio of the two TL sections and is termed to be (Z_{t2}/Z_{t1}), $X = (2\omega L_v + Z_{t1} \cdot \tan\Theta_{t1})/(Z_{t1} - 2\omega L_v \cdot \tan\Theta_{t1})$.

Moreover, any excitation can be seen as a superposition of even- and odd-mode excitations, therefore, the electrical parameters of symmetric networks can be calculated by the even- and odd-mode scattering coefficients. The S-matrix parameters of the two-port symmetric network in Fig. 5 can be obtained as

$$\begin{aligned} S_{11} = S_{22} &= \frac{Z_{in-even}Z_{in-odd} - Z_{0f}^2}{(Z_{in-even} + Z_{0f}) \cdot (Z_{in-odd} + Z_{0f})} \\ &= \frac{Y_{0f}^2 - Y_{in-even}Y_{in-odd}}{(Y_{0f} + Y_{in-even}) \cdot (Y_{0f} + Y_{in-odd})} \end{aligned} \tag{13}$$

$$\begin{aligned} S_{21} = S_{12} &= \frac{Z_{in-even}Z_{0f} - Z_{in-odd}Z_{0f}}{(Z_{in-even} + Z_{0f}) \cdot (Z_{in-odd} + Z_{0f})} \\ &= \frac{Y_{in-odd}Y_{0f} - Y_{in-even}Y_{0f}}{(Y_{0f} + Y_{in-even}) \cdot (Y_{0f} + Y_{in-odd})} \end{aligned} \tag{14}$$

where Y is the admittances of the TL equivalent circuits. By using Eq. (11) to (14), we can obtain the S-parameter results of the ECM by extracting the electrical parameters.

It is noted that the capacitance C_s is very small, the discontinuity at the step and the open edge capacitance can be neglected. Based on the formulated ECM, the transmission matrix $ABCD$ for the $\lambda/4$ SIR is (15), as shown at the bottom of the page, When the terminal is short-circuited, the input admittance Y_{in} can be expressed as

$$\begin{aligned} Y_{\text{in}} = \frac{D}{B} &= \frac{\cos\Theta_{t1}\cos\Theta_{t2} - \frac{Z_{t1}}{Z_{t2}}\sin\Theta_{t1}\sin\Theta_{t2}}{j\left(Z_{t1}\sin\Theta_{t1}\cos\Theta_{t2} + Z_{t2}\cos\Theta_{t1}\sin\Theta_{t2}\right)} \\ &= \frac{Z_{t2} - Z_{t1}\tan\Theta_{t1}\tan\Theta_{t2}}{jZ_{t2}(Z_{t1}\tan\Theta_{t1} + Z_{t2}\tan\Theta_{t2})} \end{aligned} \tag{16}$$

Then, according to the resonance condition $Y_{\text{in}} = 0$ in [34], the resonance condition of SIR can be depicted as

$$Z_{t2} - Z_{t1}\tan\Theta_{t1}\tan\Theta_{t2} = 0 \tag{17}$$

which is

$$\tan\Theta_{t1}\tan\Theta_{t2} = \frac{Z_{t2}}{Z_{t1}} = R_Z \tag{18}$$

Based on Eq. (18), the resonance condition of SIR is determined by the impedance ratio R_z and electrical lengths (Θ_{t1} and Θ_{t2},) of the TLs. On the contrary, as for the commonly used UIR, the resonance condition depends only on the electrical length of the TL, which means that the SIR has more degrees of freedom in the design than the UIR. It is worth mentioning that R_Z is an important electrical parameter that characterizes SIR features and the first few resonance frequencies can be adjusted by changing the value of R_Z. At the same time, when designing a miniaturized FSR, a smaller R_Z can be considered to obtain a smaller resonator size.

D. RESONANT FEATURES AND PARAMETRIC ANALYSIS

The effects of several key parameters on the resonant features of our FSR structure are also examined. The absorption characteristics of grounded magnetic absorber has been illustrated in Fig. 3(b). When the transmission channel is added, the port impedance Z_{0f} is increased, resulting in impedance mismatch. To analyze the influence on the absorption feature, the transmission channel is replaced by a metal block of the same size, as shown in Fig. 7(a). The reflection coefficients of the absorption channel can be calculated by Eq. (9). According to Eq. (8), the input impedance of the absorption channel is different with different values of l_a. Fig. 8(a) demonstrates that the absorption performance is improved with an increased l_a within a suitable range, on account of the matched input resistance with the port impedance. In addition, according to the previous analysis, the transmission window is determined by the electrical lengths of TLs and the impedance ratio R_Z. To facilitate the analysis, the magnetic absorber has been removed for explicit demonstration as well as the band-stop FSS, as shown in Fig. 7(b). The simulated transmission frequency with respect to different values of impedance ratio R_z has been demonstrated in Fig. 8 (b). The results are expressed through different values of h_{b2}. With a reducing value of h_{b2}, the transmission window moves to lower frequency band. It also indicated that the physical length of the channel can be reduced with smaller R_Z under the same required resonant frequency, leading to a size-miniaturized structure. Meanwhile, the remaining physical parameters are also given in the legend. Moreover, the sensitivities of other parameters on the performances can also be studied to examine the tolerances allowed in the manufacturing process through the methods described in [30].

E. DESIGN GUIDELINES

Based on the ECM and its analysis of the FSR, brief guidelines are formulated to design an FSR with a transmission window within the absorption band.

$$\begin{aligned} \begin{bmatrix} A & B \\ C & D \end{bmatrix} &= \begin{bmatrix} \cos\Theta_{t2} & jZ_{t2}\sin\Theta_{t2} \\ j\dfrac{\sin\Theta_{t2}}{Z_{t2}} & \cos\Theta_{t2} \end{bmatrix} \begin{bmatrix} \cos\Theta_{t1} & jZ_1\sin\Theta_{t1} \\ j\dfrac{\sin\Theta_{t1}}{Z_{t1}} & \cos\Theta_{t1} \end{bmatrix} \\ &= \begin{bmatrix} \cos\Theta_{t1}\cos\Theta_{t2} - \dfrac{Z_{t2}}{Z_{t1}}\sin\Theta_{t1}\sin\Theta_{t2} & j\left(Z_{t1}\sin\Theta_{t1}\cos\Theta_{t2} + Z_{t2}\cos\Theta_{t1}\sin\Theta_{t2}\right) \\ j\left(\dfrac{\cos\Theta_{t1}\sin\Theta_{t2}}{Z_{t2}} + \dfrac{\sin\Theta_{t1}\cos\Theta_{t2}}{Z_{t1}}\right) & \cos\Theta_{t1}\cos\Theta_{t2} - \frac{Z_{t1}}{Z_{t2}}\sin\Theta_{t1}\sin\Theta_{t2} \end{bmatrix} \end{aligned} \tag{15}$$

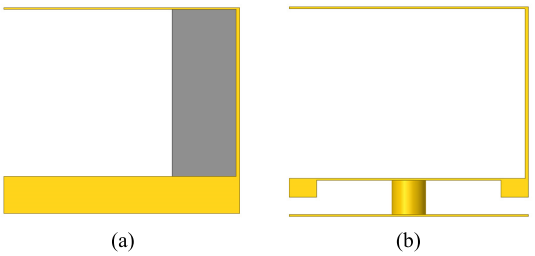

FIGURE 7. Side view of the structure for parametric analyses. (a) Analytical model of the absorption channel. (b) Analytical model of the transmission channel.

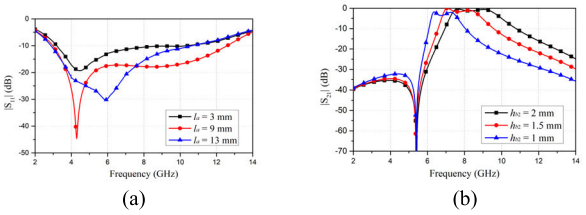

FIGURE 8. (a) Calculated reflection coefficients of the absorption channel (Physical parameters: l = 18 mm, w = 10 mm, h = 12 mm, h_a = 10 mm), (b) Calculated transmission coefficients of the transmission channel (Physical parameters: l = 15 mm, l_a = 9 mm, l_m = 3.8 mm, l_{b2} = 1.6 mm, w = 9.5 mm, h = 12 mm, h_a = 9.5 mm, h_{b1} = 2 mm, D_v = 1 mm).

1) Determine the desired frequency of the absorption bands and choose an appropriate magnetic material.
2) We assume that the transmission frequency f_t .is located in the middle of the absorption band. According to the ECM, the absorption channel can be designed. The 2D band-stop FSS with an equivalent parallel resonator (L_f and C_f), which exhibits a reflection zero at $f_t = 1/\left(2\pi\sqrt{L_f C_f}\right)$. Then, the whole absorption channel is designed for a good absorption performance.
3) Once the operating transmission frequency f_t is determined, the transmission channel can then be designed. The thickness can be approximately determined by $l \approx c/\left(2f_t\sqrt{\varepsilon_r}\right)$ when the transmission channel is implemented in the UIR structure, where ε_r represents the relative permittivity of the substrate. When it is implemented using the SIR structure, it needs to be optimized again. Generally, a larger impedance ratio R_Z is needed for a smaller thickness of the transmission channel (l). Moreover, a larger height of the transmission channel (h_{b1}) results in a wider transmission band though its selectivity may be degraded.
4) Combining the absorption and transmission channels, the FSR with desirable frequency response can then be designed.
5) The full-wave simulator HFSS or CST-MWS can be used to fine-tune the parameters of the FSR.

The above design guidelines are straightforward and quite simple to follow. The resonance frequencies can be controlled independently, and the resonance strength of each channel can also be adjusted independently. Therefore, the considerable flexibility of the guidelines can provide a convenient design process and a fast optimization procedure of the proposed FSR.

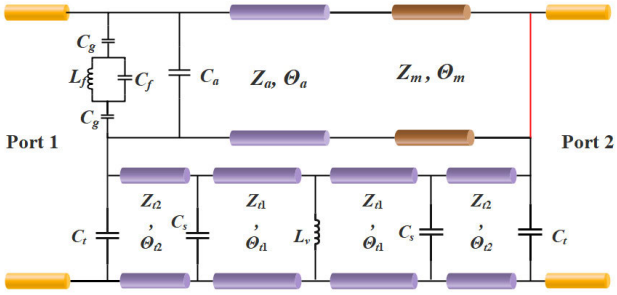

FIGURE 9. ECM of the propose FSR.

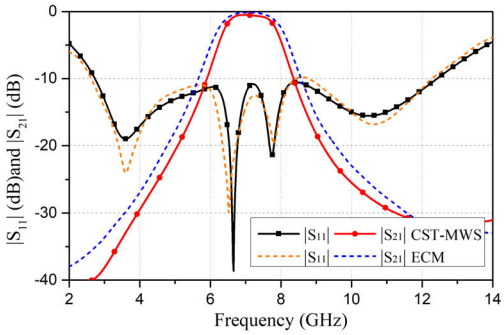

FIGURE 10. Reflection and transmission coefficients calculated by CST-MWS and ECM. (Circuit parameters: Z_{0f} = 479.1 Ω, Z_a = 377 Ω, Θ_a = 90° at 8.33 GHz, Z_{t1} = 99.2 Ω, Θ_{t1} = 90° at 15.3 GHz, Z_{t2} = 35.7 Ω, Θ_{t2} = 90° at 46.9 GHz, L_v = 0.156 nH, L_f = 14 nH, C_a = 0.08 pF, C_f = 0.008 pF, C_g = 0.07 pF, C_s = 0.006 pF, C_t = 0.017 pF).

III. FSR DESIGN EXAMPLES

To demonstrate the feasibility of the proposed design theory, a low-profile broadband FSR based on SIR with a transmission window within the absorption band is first designed and optimized. Moreover, to achieve polarization-insensitive performance, a dual-polarized example is then designed and optimized.

A. SINGLE-POLARIZED FSR

According to the description in Section II, a prototype of a single-polarized FSR with a center passband frequency of 7.1 GHz is designed at first. Fig. 2 presents the geometrical details of the unit cell. With the combination of absorption and transmission channel, the improved ECM of the proposed FSR is established and presented in Fig. 9.

The S-parameter results simulated by CST-MWS together with the results calculated by the ECM are presented in Fig. 10, where a good agreement can be observed. Both results indicate that two transmission poles appear at around 6.66 and 7.74 GHz with a sharp roll off transmission window ($|S_{21}| \geq -3$dB) from 6.36 GHz to 7.89 GHz. It can also be seen that the absorption bandwidth ($|S_{11}| \leq -10$ dB) is from 2.73 GHz to 12.43 GHz. It should be noted that the reduction of the lowest absorption frequency from 3.2 to 2.73 GHz is due to the increased input impedance caused by the band-stop FSS.

The simulated S-parameters of the single-polarized FSR under the oblique incidences and different polarizations are

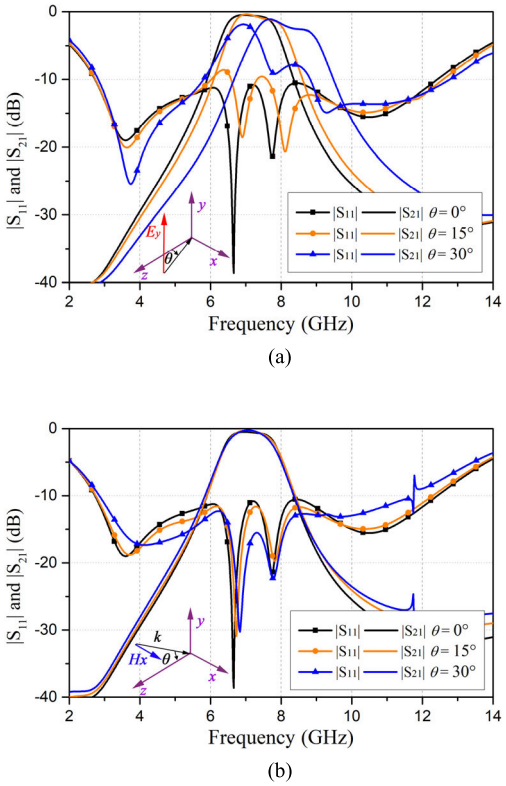

FIGURE 11. Simulated performance of the single-polarized FSR under the oblique incidence. (a) Under the oblique incidence in the *xz* plane (0°, θ). (b) Under the oblique incidence in the *yz* plane (90°, θ).

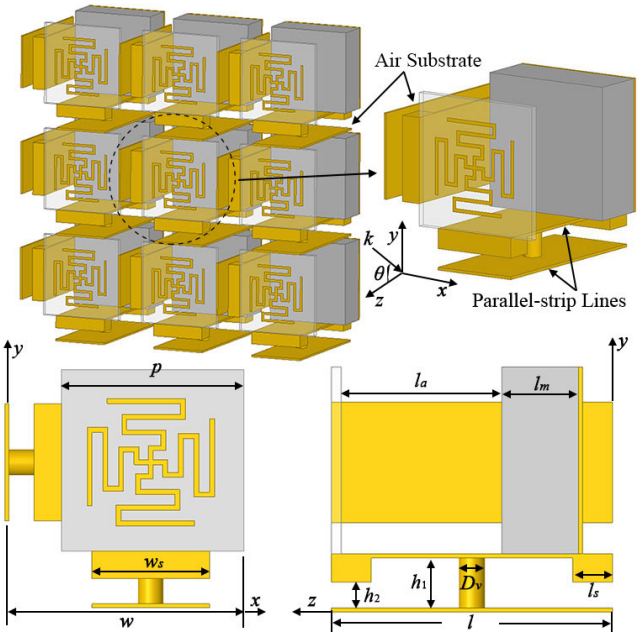

FIGURE 12. Perspective view of the proposed FSR and geometrical details of the unit cell. (Physical dimensions: D_v = 1.3 mm, h_1 = 2.5 mm, h_2 = 1.3 mm, l = 14 mm, l_a = 7.5 mm, l_m = 3.8 mm, l_s = 1.6 mm, p = 9.5 mm, w = 12 mm, w_s = 6 mm).

investigated and plotted in Fig. 11. It illustrated the oblique incidence scanned in the *xz* (0°, θ) and *yz* (90°, θ) planes, respectively. It is noted that the frequency responses are stable and the characteristics under oblique incident angle scanned in the *yz* plane is more stable compared with the *xz* plane. As shown in Fig. 11(a), the transmission window shifts to a higher frequency along with an increasing incident angle due to the decreased effective electrical length viewed from the oblique incidence. Moreover, the characteristic impedances will also be changed with the incident angle, leading to a degraded performance. For a better stability, smaller dimension of the unit cell size may be used through loading and bending techniques.

B. DUAL-POLARIZED FSR

Based on the above single-polarized FSR, a dual-polarized design is further proposed. Fig. 12 provides the geometry of the proposed dual-polarized FSR, which is modified from the single-polarized one. The structure is symmetrical and distributed both in the *x*- and *y*-axes for dual-polarized FSR, ensuring that the structure has the same performance under both TE and TM polarizations. In this design, the band-stop FSS in the absorption channel is also constructed by a rotationally symmetric meander line to guarantee the good performance for both *x*- and *y*-polarized incident plane waves. The transmission channels are placed around the absorption channels and are formed by parallel-strip lines inserted with SIR structure and metallic vias.

The simulated *S*-parameter results of the proposed dual-polarized FSR for both TE and TM polarizations under the normal incidence are exhibited in Fig. 13, where the results calculated by ECM have also be shown. It is obvious that the relevant curves fit well, which demonstrates that the construction has identical function for both polarizations. Therefore, one polarization state can be carried out to simplify the design and experimental process similar to the single-polarized one. The center frequency of the operating passband is 7.25 GHz with a transmission window ($|S_{21}| \geq -3$dB) ranging from 6.33 to 8.18 GHz and the absorption bandwidth ($|S_{11}| \leq -10$ dB) is from 3.45 to 14 GHz. It should be noted that the ECM in Fig. 9 is only based on two fundamental modes. It may be mentioned that the ECM can only be used to predict the performance approximately, not very accurately. In addition, the couplings between the rotational symmetry structures for TE and TM polarizations cannot be considered in the ECM. All these reasons lead to some differences between full-wave simulation and equivalent model. The frequency responses of the dual-polarized FSR under the oblique incidence are also studied and shown in Fig. 14. As mentioned above, it only shows the results under the TE polarization and the oblique incidence scanned in the *xz* (0°, θ) plane. The results are the same under the TM polarization and the oblique incidence scanned in the *yz* (0°, θ) plane due to the completely symmetrical structure. Stable performances can be observed with the increasing incident angle because of the relatively small dimension of the unit cell.

It should be mentioned that better angular stability can be achieved by reducing the size of the unit cell for both of our

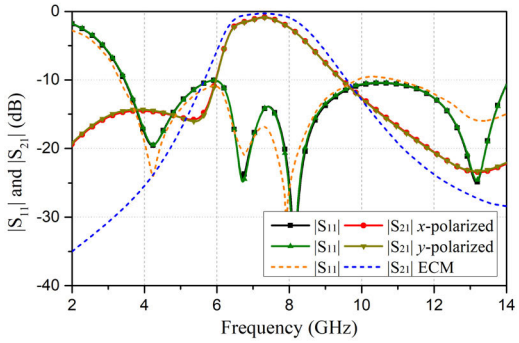

FIGURE 13. Simulated results of the dual-polarized FSR for both x - and y-polarized incident waves from the CST-MWS and ECM (Circuit parameters: $Z_{0f} = 479.1\ \Omega$, $Z_a = 377\ \Omega$, $\Theta_a = 90°$ at 10 GHz, $Z_{t1} = 78.5\ \Omega$, $\Theta_{t1} = 90°$ at 13.9 GHz, $Z_{t2} = 40.8\ \Omega$, $\Theta_{t2} = 90°$ at 46.9 GHz, $L_v = 0.148$ nH, $L_f = 17.3$ nH, $C_a = 0.04$ pF, $C_f = 0.015$ pF, $C_g = 0.05$ pF, $C_s = 0.006$ pF, $C_t = 0.005$ pF).

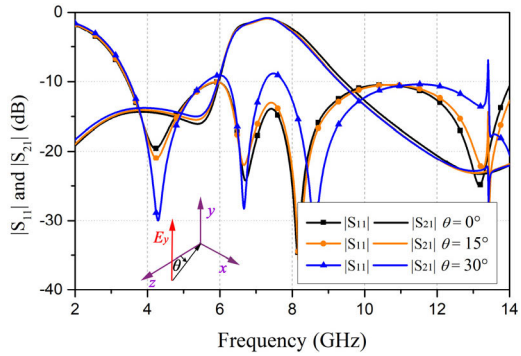

FIGURE 14. Simulated reflection and transmission coefficients of the dual-polarized FSR under various incident angles in the xz plane (0°, θ).

FSR structures, which also requires consideration of the cost and manufacturing tolerance.

IV. FABRICATION AND MEASUREMENT

To verify the design concept and simulated results, prototypes of the proposed FSRs are fabricated and tested employing a parallel-plate waveguide set-up, which is an efficient way to characterize the periodic structures, as described in [2].

A. SINGLE-POLARIZED FSR

A prototype of the proposed single-polarized FSR is fabricated to validate our design, as shown in Fig. 15(b). It contains ten cells along the horizontal axis with a total size of 95 mm × 12.6 mm approximately. The thickness is $0.118\lambda_L$, where λ_L is the free-space wavelength at the lowest frequency of the absorption band. Herein, the 2D band-stop FSS is printed on one-layer of Rogers 5880 substrate with a thickness of 0.508 mm. In the fabrication, according to previous research, the challenge is the accuracy of metallic via, which is important for the filtering performance and should be careful manufactured. As shown in Fig. 16, the sample is measured in a parallel-plate waveguide set-up, which is an efficient way to characterize the periodic structures under the normal

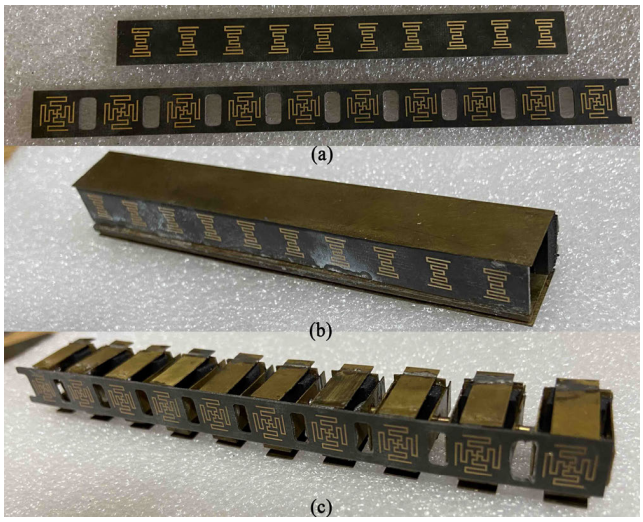

FIGURE 15. Fabricated prototype of the proposed FSR. (a) Constructions of the two band-stop FSSs. (b) Single-polarized FSR. (c) Dual-polarized FSR.

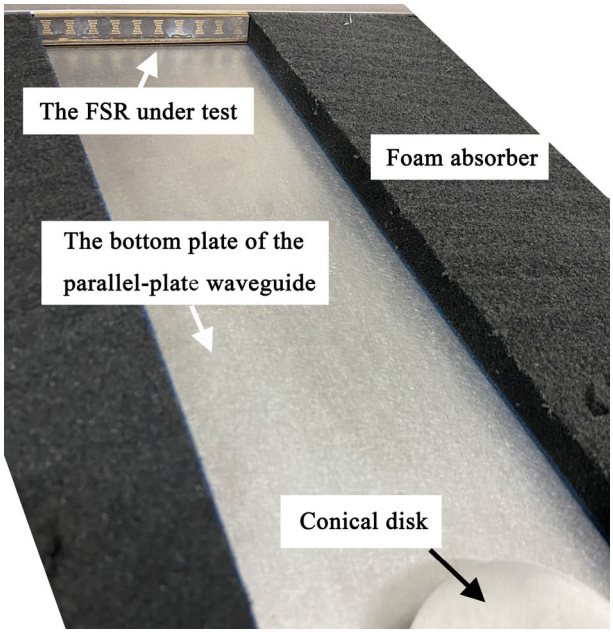

FIGURE 16. Fabricated FSR within the measurement setup.

incidence and the measurement procedures were described in detail in [2]. A comparison between the measured and simulated reflection and transmission coefficients under the normal incidence is shown in Fig. 17. It is seen that the simulated and measured results are in good agreement. The measured insertion loss is 0.83 dB, slightly higher than the simulated one, and the measured reflection coefficient has some deviations from the simulated ones especially at high frequency. These differences may come from the inaccuracy of fabrication and errors in the assembling process. It is concluded that this structure performs high selectivity feature with a broad absorption band.

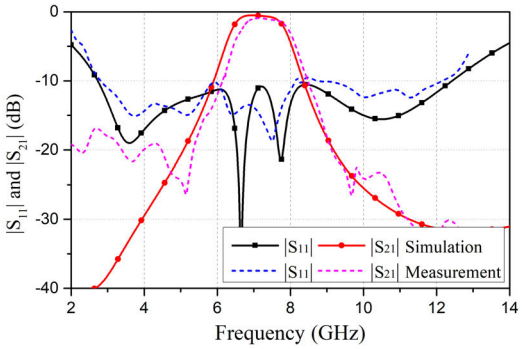

FIGURE 17. Simulated and measured results of the fabricated single-polarized FSR under the normal incidence.

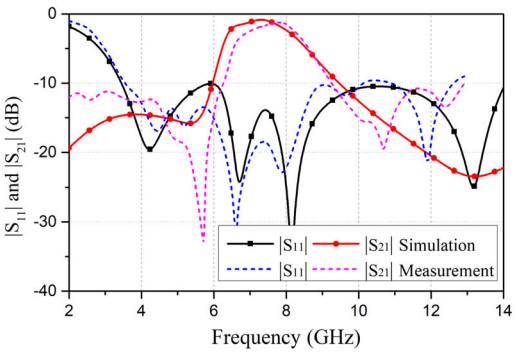

FIGURE 18. Simulated and measured results of the fabricated dual-polarized FSR under the normal incidence.

B. DUAL-POLARIZED FSR

For demonstration, a sample of the dual-polarized FSR prototype is also fabricated and measured. Fig. 15(c) shows the photograph of our fabricated sample with a 10 × 1 array and the physical dimension of the unit cell has been exhibited in Fig. 12. The total size is approximately 122 mm × 12.2 mm and the thickness is about $0.158\lambda_L$, where λ_L is the free-space wavelength at the lowest frequency of the absorption band. In addition, as we discussed before, this structure is symmetrical and the performances under TE and TM polarizations are the same under the normal incidence. Hence, only one polarization can be considered to simplify the experiment. The measurement process is the same as the previous single-polarized one. The measured reflection and transmission coefficients of the dual-polarized FSR under the normal incidence are shown in Fig. 18. Good agreement can be observed between the measured and simulated results, while the small difference is attributed to the manufacturing errors. The minimum insertion loss of the measured passband is 1.26 dB. Compared with the single-polarized structure, the dual-polarized one also represents low-profile and broadband absorption properties and improve the polarization characteristics simultaneously. However, it should be mentioned that the performance characteristics of the dual-polarized FSR is inevitably degraded compared with the single-polarized one because of design constrains and more assembly errors faced by dual-polarized design. Furthermore, it is still a challenge for the dual-polarized FSR to design a simple and efficient reconfigurable method without scarifying other performances.

Finally, to clearly understand the performances and advantages of our proposed single- and dual-polarized 3-D FSRs, a comparison with other reported designs is listed in Table 1. Obviously, our presented FSRs have wideband absorption and thin thickness characteristics at the same time. The performance of the dual-polarized FSR is similar with that of the single-polarized one. It is clear that our design has advantages in the wide absorption bandwidth and mechanical stability compared with the 2-D structure. For 3-D structures, the thin thickness owe to the SIR structure and the dual polarization characteristics caused by the rotationally symmetric structure

TABLE 1. Comparisons between our proposed FSR and previously reported FSR designs.

Ref.	Transmission bandwidth	Absorption bandwidth	Thickness (λ_L)[1]	Number of lumped components	Structure	Polarization
[7]	10%	99%	0.12	4	2-D	Dual
[9]	N.A.	98.3%	0.13	4	2-D	Dual
[17]	38%	92.8%	0.13	6	2-D	Dual
[2]	20%	92.8%	0.16	9	3-D	Single
[21]	8.4%	64%	0.31	1	3-D	Single
[23]	42.7%	104%	0.2	2	3-D	Dual
Our work	22.6%	128%	0.118	0	3-D	Single
	25.5%	121.1%	0.158	0	3-D	Dual

[1] λ_L is the free-space wavelength at the lowest frequency of the absorption band.

are accomplished in our design. Moreover, an appropriate transmission bandwidth ($|S_{21}| \geq -3$dB) and a low insertion loss can be obtained for both FSRs. Furthermore, the lumped-element-free feature can highly reduce the complexity of the manufacturing process and minimize assembly errors.

V. CONCLUSION

In this article, a new design of low-profile 3-D FSR with two-sided wide absorption bands and no lumped components has been proposed and investigated by utilizing a wideband magnetic material with cascaded band-stop and 3-D FSS. Printed band-stop FSS array is applied to reduce the insertion loss and avoid the extra lumped components. ECM together with odd-even mode analysis method has been introduced to demonstrate and analyze the operational principles in detail. Furthermore, to expand the effectiveness of the design strategy and improve the polarization-insensitive performance, one dual-polarized FSR is then presented. Both prototypes have been designed, fabricated and experimentally verified. The measured results are in good agreement with the simulated ones. It should be mentioned that only the measurement under the normal incidence is implemented in the current parallel-plate waveguide set-up. The results of oblique incidence performance can be measured through the free-space

test method. However, a large array should be implemented in the free-space measurements. The proposed FSRs are expected to find potential applications in some military radar systems. It should be noted that the passband can be tuned by altering the resonances of the transmission channel and the band-stop FSS in front of the absorbing material, including the introduction of liquid crystals and other reconfigurable methods. Some future work may be considered to investigate such tunable feature and eventual integration with antennas to realize out-of-band RCS reduction.

REFERENCES

[1] B. A. Munk, *Metamaterials: Critique and Alternatives*. Hoboken, NJ, USA: Wiley, 2009.
[2] A. A. Omar, Z. Shen, and H. Huang, "Absorptive frequency-selective reflection and transmission structures," *IEEE Trans. Antennas Propag.*, vol. 65, no. 11, pp. 6173–6178, Nov. 2017.
[3] H. Huang and Z. Shen, "Absorptive frequency-selective transmission structure with square-loop hybrid resonator," *IEEE Antennas Wireless Propag. Lett.*, vol. 16, pp. 3212–3215, Nov. 2017.
[4] A. A. Omar, J. Kim, and W. Hong, "A 3-D lumped-components-free absorptive frequency-selective transmission structure featuring very wide two-sided absorption bandwidths," *IEEE Antennas Wireless Propag. Lett.*, vol. 19, no. 5, pp. 761–765, May 2020.
[5] Q. Chen, L. Liu, L. Chen, J. Bai, and Y. Fu, "Absorptive frequency selective surface using parallel LC resonance," *Electron. Lett.*, vol. 52, no. 6, pp. 418–419, Mar. 2016.
[6] Q. Chen, S. Yang, J. Bai, and Y. Fu, "Design of absorptive/transmissive frequency-selective surface based on parallel resonance," *IEEE Trans. Antennas Propag.*, vol. 65, no. 9, pp. 4897–4902, Sep. 2017.
[7] M. Guo, Q. Chen, T. Bai, K. Wei, and Y. Fu, "Wide transmission band frequency-selective Rasorber based on convoluted resonator," *IEEE Antennas Wireless Propag. Lett.*, vol. 19, no. 5, pp. 846–850, May 2020.
[8] M. Guo, Q. Chen, D. Sang, Y. Zheng, and Y. Fu, "Dual-polarized dual-band frequency selective rasorber with low insertion loss," *IEEE Antennas Wireless Propag. Lett.*, vol. 19, no. 1, pp. 148–152, Jan. 2020.
[9] M. Guo, T. Guo, Q. Chen, Y. Zheng, and Y. Fu, "Frequency selective rasorber with anisotropic transmission band," *IEEE Antennas Wireless Propag. Lett.*, early access, Dec. 3, 2020, doi: 10.1109/LAWP.2020.3042308.
[10] F. Costa and A. Monorchio, "A frequency selective radome with wideband absorbing properties," *IEEE Trans. Antennas Propag.*, vol. 60, no. 6, pp. 2740–2747, Jun. 2012.
[11] W. S. Arceneaux, R. D. Akins, and W. B. May, "Absorptive/transmissive radome," U.S. Patent 5 400 043, Mar. 21, 1995.
[12] Y. Han, W. Che, X. Xiu, W. Yang, and C. Christopoulos, "Switchable low-profile broadband frequency-selective rasorber/absorber based on slot arrays," *IEEE Trans. Antennas Propag.*, vol. 65, no. 12, pp. 6998–7008, Dec. 2017.
[13] L. Wu, S. Zhong, J. Huang, and T. Liu, "Broadband frequency-selective rasorber with varactor-tunable interabsorption band transmission window," *IEEE Trans. Antennas Propag.*, vol. 67, no. 9, pp. 6039–6050, Sep. 2019.
[14] Y. Shang, Z. Shen, and S. Xiao, "Frequency-selective rasorber based on square-loop and cross-dipole arrays," *IEEE Trans. Antennas Propag.*, vol. 62, no. 11, pp. 5581–5589, Nov. 2014.
[15] Y. Hu, S. Liu, X. Kong, and C. Mao, "Low windage resistance frequency-selective rasorber based on windmill-shape coupling line arrays," *Electron. Lett.*, vol. 53, no. 22, pp. 1450–1452, Oct. 2017.
[16] S. C. Bakshi, D. Mitra, and F. L. Teixeira, "FSS-based fully reconfigurable rasorber with enhanced absorption bandwidth and simplified bias network," *IEEE Trans. Antennas Propag.*, vol. 68, no. 11, pp. 7370–7381, Nov. 2020.
[17] W. Yu, G. Q. Luo, Y. Yu, Y. Pan, W. Cao, Y. Pan, and Z. Shen, "Dual-polarized band-absorptive frequency selective rasorber using meander-line and lumped resistors," *IEEE Trans. Antennas Propag.*, vol. 67, no. 2, pp. 1318–1322, Feb. 2019.
[18] Q. Guo, Z. Li, J. Su, L. Y. Yang, and J. Song, "Dual-polarization absorptive/transmissive frequency selective surface based on tripole elements," *IEEE Antennas Wireless Propag. Lett.*, vol. 18, no. 5, pp. 961–965, May 2019.
[19] Q. Chen, D. Sang, M. Guo, and Y. Fu, "Miniaturized frequency-selective rasorber with a wide transmission band using circular spiral resonator," *IEEE Trans. Antennas Propag.*, vol. 67, no. 2, pp. 1045–1052, Feb. 2019.
[20] X. Xiu, W. Che, Y. Han, and W. Yang, "Low-profile dual-polarization frequency-selective rasorbers based on simple-structure lossy cross-frame elements," *IEEE Antennas Wireless Propag. Lett.*, vol. 17, no. 6, pp. 1002–1005, Jun. 2018.
[21] Y. Han, L. Zhu, Y. Chang, and B. Li, "Dual-polarized bandpass and band-notched frequency-selective absorbers under multimode resonance," *IEEE Trans. Antennas Propag.*, vol. 66, no. 12, pp. 7449–7454, Dec. 2018.
[22] Z. Wang, Q. Zeng, J. Fu, W. Chen, B. Lv, M. Song, and T. A. Denidni, "A high-transmittance frequency-selective rasorber based on dipole arrays," *IEEE Access*, vol. 6, pp. 31367–31374, 2018.
[23] Z. Sun, Q. Chen, M. Guo, H. Yu, and Y. Fu, "Frequency selective rasorber and reflector with two-sided absorption bands," *IEEE Access*, vol. 7, pp. 6025–6031, 2019.
[24] X. Yan, X. Kong, Q. Wang, L. Xing, F. Xue, Y. Xu, S. Jiang, and X. Liu, "Water-based reconfigurable frequency selective rasorber with thermally tunable absorption band," *IEEE Trans. Antennas Propag.*, vol. 68, no. 8, pp. 6162–6171, Aug. 2020.
[25] B. Li and Z. Shen, "Wideband 3D frequency selective rasorber," *IEEE Trans. Antennas Propag.*, vol. 62, no. 12, pp. 6536–6541, Dec. 2014.
[26] Y. Yu, G. Q. Luo, A. A. Omar, X. Liu, W. Yu, Z. C. Hao, and Z. Shen, "3D absorptive frequency-selective reflection and transmission structures with dual absorption bands," *IEEE Access*, vol. 6, pp. 72880–72888, Dec. 2018.
[27] Z. Shen, J. Wang, and B. Li, "3D frequency selective rasorber: Concept, analasis, and design," *IEEE Trans. Microw. Theory Techn.*, vol. 64, no. 10, pp. 3087–3096, Oct. 2016.
[28] Y. Yu, Z. Shen, T. Deng, and G. Luo, "3-D frequency-selective rasorber with wide upper absorption band," *IEEE Trans. Antennas Propag.*, vol. 65, no. 8, pp. 4363–4367, Aug. 2017.
[29] T. Deng, Y. Yu, Z. Shen, and Z. N. Chen, "Design of 3-D multilayer ferrite-loaded frequency-selective rasorbers with wide absorption bands," *IEEE Trans. Microw. Theory Techn.*, vol. 67, no. 1, pp. 108–117, Jan. 2019.
[30] Y. Yu, G. Q. Luo, Q. Liu, W. Yu, H. Jin, Z. Liao, and Z. Shen, "3D band-absorptive frequency selective rasorber: Concept and analysis," *IEEE Access*, vol. 7, pp. 2520–2528, Dec. 2019.
[31] Y. Wang, S. Qi, W. Wu, and Z. Shen, "An ultra-thin wideband 3-D frequency selective rasorber based on ferrite absorber and slow wave structure," in *Proc. IEEE Int. Symp. Antennas Propag. USNC-URSI Radio Sci. Meeting*, Atlanta, GA, USA, Jul. 2019, pp. 957–958.
[32] Y. Wang, S.-S. Qi, Z. Shen, and W. Wu, "Ultrathin 3-D frequency selective rasorber with wide absorption bands," *IEEE Trans. Antennas Propag.*, vol. 68, no. 6, pp. 4697–4705, Jun. 2020.
[33] M. Sagawa, M. Makimoto, and S. Yamashita, "Geometrical structures and fundamental characteristics of microwave stepped-impedance resonators," *IEEE Trans. Microw. Theory Techn.*, vol. 45, no. 7, pp. 1078–1085, Jul. 1997.
[34] M. Makimoto and S. Yamashita, *Microwave Resonators and Filters for Wireless Communications-Theory and Design*. Berlin, Germany: Springer-Verlag, 2001.

YIHAO WANG was born in Xi'an, Shaanxi, China, in 1992. He received the B.Eng. degree from the School of Electronic and Information Engineering, Beihang University, Beijing, China, in 2014. He is currently pursuing the Ph.D. degree in information and communication engineering with the School of Electronic and Optical Engineering, Nanjing University of Science and Technology, China.

His current research interests include microwave circuit analog absorber, frequency selected surface, and absorber measurement.

MIN WANG (Member, IEEE) was born in Jiangsu, China, in July 1972. She received the B.Eng. degree in radio engineering and the Ph.D. degree in electronic engineering from the Nanjing University of Science and Technology, Nanjing, China, in 1994 and 1999, respectively.

Since 2003, she has been an Associate Professor with the School of Electronic and Optical Engineering, Nanjing University of Science and Technology. Her current research interests include microstrip antennas and circuits, leaky-wave antennas, and ultra-band wide-scanning array antennas.

ZHONGXIANG SHEN (Fellow, IEEE) received the B.Eng. degree in electrical engineering from the University of Electronic Science and Technology of China, Chengdu, China, in 1987, the M.S. degree in electrical engineering from Southeast University, Nanjing, China, in 1990, and the Ph.D. degree in electrical engineering from the University of Waterloo, Waterloo, ON, Canada, in 1997.

From 1990 to 1994, he was with the Nanjing University of Aeronautics and Astronautics, Nanjing. He joined Com Dev Ltd., Cambridge, ON, as an Advanced Member of Technical Staff, in 1997. In 1998, he joined the Gordon McKay Laboratory, Harvard University, Cambridge, MA, USA, and then the Radiation Laboratory, University of Michigan, Ann Arbor, MI, USA, as a Postdoctoral Fellow. In 1999, he joined Nanyang Technological University, Singapore, as an Assistant Professor, where he is currently a Full Professor. He has authored or coauthored more than 170 journal articles (among them 100 were published in IEEE journals) and presented more than 160 conference papers. His current research interests include the design of small and planar antennas for various wireless communication systems, analysis and design of frequency-selective structures, and hybrid numerical techniques for modeling RF/microwave components and antennas.

Dr. Shen has served as the Chair for the IEEE MTT/AP Singapore Chapter in 2009. He was the Chair of the IEEE AP-S Chapter Activities Committee from 2010 to 2014. He is currently the Secretary of the IEEE AP-S and an Associate Editor of the IEEE TRANSACTIONS ON ANTENNAS AND PROPAGATION.

WEN WU (Senior Member, IEEE) received the Ph.D. degree in electromagnetic field and microwave technology from Southeast University, Nanjing, China, in 1997.

He is currently a Professor with the School of Electronic Engineering and Optoelectronic Technology, Nanjing University of Science and Technology, Nanjing, where he is also the Associate Director of the Ministerial Key Laboratory of JGMT. He has authored or coauthored more than 60 journal and conference papers and has submitted five patent applications. His current research interests include microwave- and millimeter-wave theories and technologies, microwave and millimeter-wave detection, and multimode compound detection.

Dr. Wu was a recipient of six times of the Ministerial and Provincial-Level Science and Technology Awards.